

Ultrasensitive Organic-Modulated CsPbBr₃ Quantum Dot Photodetectors via Fast Interfacial Charge Transfer

Jingzhou Li, Junmin Xia, Yuan Liu, Siwei Zhang, Changjiu Teng, Xuan Zhang, Bilu Liu, Shichao Zhao, Shixi Zhao, Baohua Li, Guichuan Xing, Feiyu Kang, and Guodan Wei*

The integration of organic materials with colloidal quantum dots (QDs) has the merits the advantages of the molecular diversity and photoelectric tunability for ultrasensitive photodetector applications. Herein, a uniform CsPbBr₃ QD layer is sandwiched between the same poly-(N, N'-bis-4-butylphenyl-N, N'-bisphenyl) benzidine (Poly-TPD) and phenyl-C61-butyric acid methyl ester (PCBM) (1:1) organic blend films. The CsPbBr₃ QD layer efficiently absorbs the excitation light, where the generated exciton can sufficiently diffuse to the interface of QD and organic blend layers for efficient charge separation and effective gate modulation. Owing to the desirable heterojunction at the interface, the dark current is substantially suppressed, while the photocurrent is increased in comparison with those of pristine QDs photodetectors. The ultrafast charge transfer time (≈ 300 ps) from QDs to organic blend layer measured by the time-resolved transient absorption spectroscopy is potentially benefit the enhanced electron-hole pair dissociation. The solution-processed, organic (Poly-TPD:PCBM blend)-modulated CsPbBr₃ QDs photodetector are exhibited ultrasensitive photoresponse abilities in terms of noise equivalent power ($NEP = 1 \times 10^{-16} \text{ W Hz}^{-0.5}$), $I_{\text{Light}}/I_{\text{Dark}}$ ratio (2×10^3), and the specific detectivity ($D^* = 4.6 \times 10^{13} \text{ Jones}$). The results will be a starting point for ultrasensitive next-generation light detection technologies.

Dr. J. Li, S. Zhang, C. Teng, Prof. X. Zhang, Prof. B. Liu, Prof. F. Kang, Prof. G. Wei

Tsinghua-Berkeley Shenzhen Institute (TBSI)

Tsinghua University

Shenzhen 518055, China

E-mail: weiguodan@sz.tsinghua.edu.cn

Dr. J. Li, Y. Liu, S. Zhang, C. Teng, Prof. X. Zhang, Prof. B. Liu, Prof. S. Zhao, Prof. B. Li, Prof. F. Kang, Prof. G. Wei

Tsinghua Shenzhen International Graduate School

Tsinghua University
Shenzhen 518055, China

J. Xia, Prof. G. Xing

Institute of Applied Physics and Materials Engineering

University of Macau

Macau S.A.R. 999078, China

Prof. S. Zhao

College of Materials and Environmental Engineering

Hangzhou Dianzi University

Hangzhou 310018, China

 The ORCID identification number(s) for the author(s) of this article can be found under <https://doi.org/10.1002/admi.201901741>.

DOI: 10.1002/admi.201901741

1. Introduction

Photodetectors, devices that convert photons to electricity, are attracting increasing interest in wide range of applications including artificial intelligence, optical communication, and industrial inspection.^[1–12] Commercial photodetectors are still dominated by traditional semiconductor materials, such as Si, Ge, and InGaAs. However, due to their limitation of lattice quality, manufacture and theoretical limit of materials, it is relatively difficult to substantially tune the photoelectric properties of these materials. Especially, the mechanical inflexibility is a huge challenge to meet the growing demands for broad applications and new technologies for flexible and wearable electronics. As opposed to most inorganic counterparts, organic materials have significant advantages of facile solution processability on plastics as well as the chemically functionalized capability, allowing for extremely thin, lightweight, and conformable products. Therefore, owing to their excellent flexibility, tailororable optoelectronic properties

tunability, organic materials are one of the suitable materials to vertically stack together with colloidal quantum dots (QDs) to form an energy favorable organic/inorganic heterojunction, facilitating an effective interface for charge carrier separation. Recently, researchers have been intensively carried out to combine active QDs with organic materials to form energy favorable junctions for photodetector applications.^[13]

Colloidal QDs can also be easily solution processible in ambient condition for integration onto various substrates,^[14–17] and have exhibited excellent potential in photodetection owing to their broad absorption spectrum from the UV to mid-infrared, high absorption coefficient, and outstanding photoelectric tunability.^[18–21] In general, high performance photodetectors require effective charge transport of photogenerated carriers for signal sensitivity and significant suppression of low dark current for minimal noise. Typically, charge transport in QDs solid film is realized by carrier hopping between adjacent QDs, which is strongly dependent on their interdistance. To improve the interparticle charge transport, researchers try to substitute long-chain ligands with shorter ones.^[21–23] However,

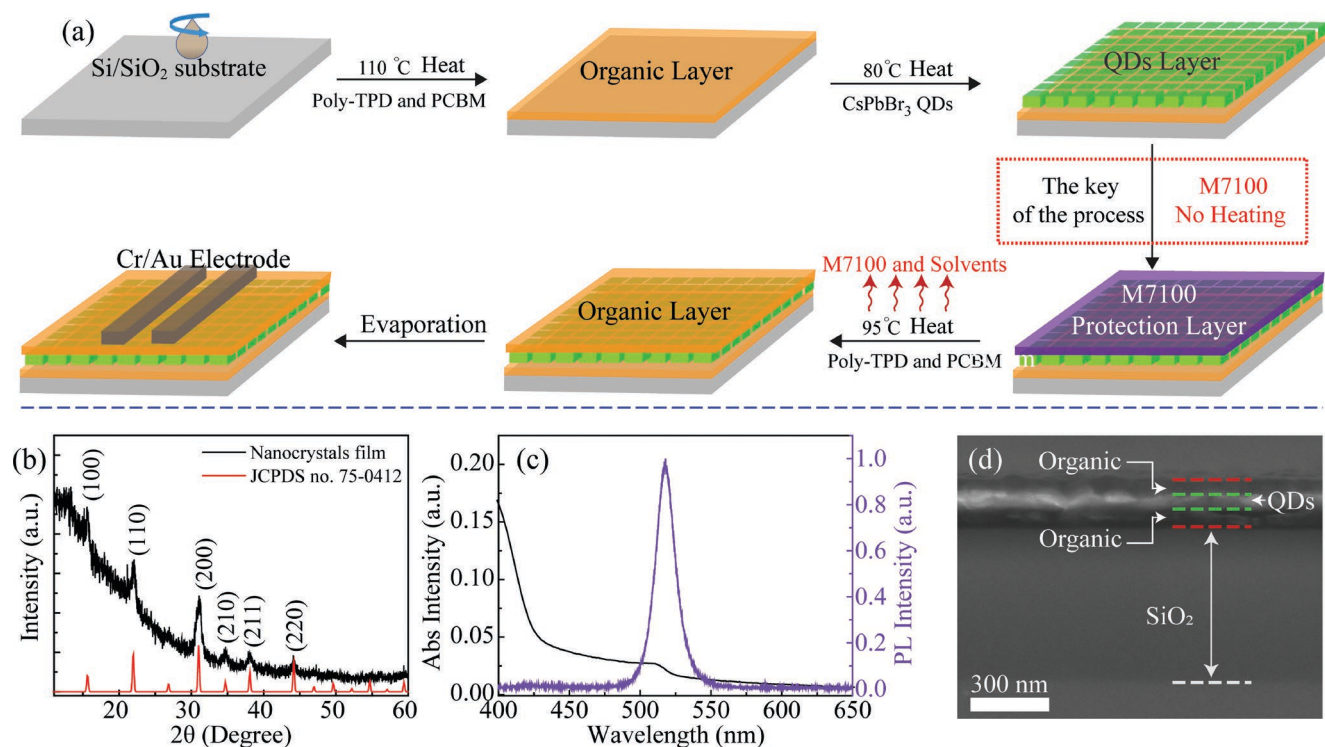


Figure 1. Fabrication and properties of the organic–inorganic perovskite QDs hybrid photodetector. a) Schematic illustration of the preparation of the hybrid photodetectors. b) XRD patterns of the CsPbBr₃ QDs film. It indicated that the perovskite QDs is cubic phase. c) Absorption spectra (black) and PL spectra (violet) of the sandwich structure on quartz substrate. The absorption and PL peak of the device are 512 and 517 nm, respectively. d) Cross-sectional SEM image showing the device architecture: p-type Si/SiO₂ (300 nm)/organic layer (about 43 nm)/QDs film (about 32 nm)/organic layer (about 30 nm).

this method is usually accompanied by a large dark current due to interfacial traps of the assembled films, which severely limits its signal detection ability. Other options, such as blending QD materials with organic materials could facilitate the fast electron charge transfer from inorganic QD to fullerene, resulting increased photocurrent. But holes usually are trapped in the nanocrystals with this strategy due to no effective hole transport layer available nearby.^[24–27] Thus, it is still a challenge for seeking QDs photodetectors, which exhibit high photocurrent with suppression of dark current.

In this paper, we designed a multilayer photodetector by sandwiching a uniform layer of CsPbBr₃ QDs film between two same organic blend films, which are mixed with a hole transport material (poly-(N, N'-bis-4-butylphenyl-N, N'-bisphenyl) benzidine, Poly-TPD) and an electron transport material (phenyl-C61-butyric acid methyl ester, PCBM). This device is fabricated by adding a protecting layer deposited from hydrofluoroether solution (M7100) between the QDs film and the organic layer to solve the challenge of solvent orthogonality. The energy levels of this blend organic films were effectively modulated by adjusting the ratio of these Poly-TPD and PCBM components. Owing to the heterojunction formed at the interface of the organic/inorganic films, the dark current is substantially suppressed, while the photocurrent is increased in comparison with those of pristine QDs and pristine organic/QDs photodetectors. The charge transfer time from CsPbBr₃ QDs to organic layers has been characterized to about 300 ps.

Outstanding photoresponse properties, such as detectivity (4.6×10^{13} J), noise equivalent power (1×10^{-16} W Hz^{-0.5}) and $I_{\text{Light}}/I_{\text{Dark}}$ ratio (2×10^3), making organic-modulated CsPbBr₃ QDs to be promising photodetectors.

2. Results

A fabrication diagram of the proposed organic-QDs photodetectors is shown in Figure 1a and the procedure is described in detail in the Experimental Section. The challenges of making all-solution processed QDs photodetectors is that the ultrathin QDs film could be partially dissolved or damaged by the subsequent solvent (such as chlorobenzene) dissolved with the following organic materials, resulting discontinuous morphologies. To target damage-free and all-solution processed photodetectors, a hydrofluoroether (3M Novec 7100, M7100) solution has been introduced as a protective layer for CsPbBr₃ QDs layer and it can be completely evaporated along with the subsequent thermal annealing process. The impact of M7100 on devices fabrication is described in detail in Section S1 (Supporting Information). Heavily p-doped Si wafer with thermally grown 300 nm SiO₂ layer was used as the gate/dielectric and substrates. Transmission electron microscopy (TEM) image of CsPbBr₃ QDs indicate a highly crystalline and uniform cubic morphology with an average size of about 16 nm (Figure S3, Supporting Information). From the X-ray diffraction (XRD)

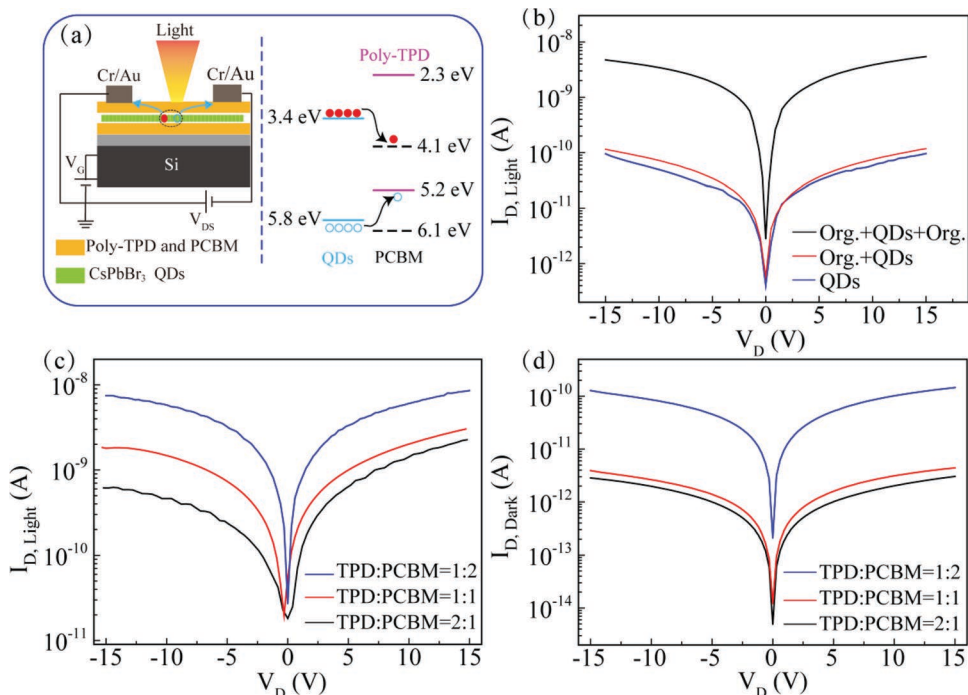


Figure 2. Photoresponse characteristics of organic-modulated QDs photodetector. a) Schematic diagram of the organic-QDs photodetector (left). Energy level diagram of the CsPbBr_3 QDs, Poly-TPD, and PCBM (right).^[28,29] b) $I_{\text{D}, \text{Light}}$ - V_{D} characteristics of three devices with substrate/organic/QDs/organic/electrode, substrate/organic/QDs/electrode structure, and substrate/organic/electrode structure, respectively. c-d) The photocurrent and dark current of three devices with different mass ratios of organic materials.

patterns of the CsPbBr_3 QDs film (Figure 1b), we can find the (100), (110), (200), (210), and (220) peaks, which demonstrated that the CsPbBr_3 QDs remains cubic phase (JCPDS no. 75-0412). Figure 1c shows the absorption peak (black) of 512 nm and photoluminescence (PL) peak (violet) of 517 nm for the sanwiched structure on quartz substrate, respectively. The thickness of the QDs film is about 32 nm, which corresponds to two layers of QDs (Figure 1d).

The photoresponse of the organic-modulated QDs photodetectors were investigated by top illumination with a 450 nm monochromatic light onto the entire region of the device (Figure 2a). Here, the channel width of the device is 20 μm and the length is 100 μm . The photocurrent of this novel organic/QDs/organic sandwiched device exhibits up to 50 times higher than those of single-layer QDs and organic/QDs/electrode photodetectors (Figure 2b). Here, we also constructed multilayer devices with different organic blend components (the Poly-TPD and PCBM are mixed by various mass ratios). It is important to note that the device with organic ratio of 1:1 presents high photocurrent with significant suppression of dark current (Figure 2c,d). Contrary to the photoresponse for 1:1 device, the ratio of 1:2 one shows extremely high dark current. This reason will be analyzed in detail in the Discussion section.

The photoresponse ability of the Poly-TPD:PCBM = 1:1 device was further systematically studied. The output $I_{\text{D}}-V_{\text{D}}$ characteristics in dark and under the light irradiance of 0.14 mW cm^{-2} , $V_{\text{G}} = 0$ are shown in Figure 3a. The device exhibits a low dark current of $2.4 \times 10^{-12} \text{ A}$ at a bias of 15 V. At the same time, the dark current is symmetric around $V_{\text{D}} = 0$ and show a linear voltage dependence (Figure S4, Supporting Information).

According to $V_{\text{D}} = I_{\text{D}}R$, the R of the device is about 586 G Ω . Single-layer organic photodetectors were also fabricated, and it shows similar the dark current to those of multilayer devices (Figure S5, Supporting Information). This indicates that the dark current of the photodetector is dominated by charge transport in organic layer driven by electric field due to relatively low electron and hole mobility. There is also no obvious photocurrent of single-layer organic structure photodetectors (Figure S6, Supporting Information), which is attributed to the fact that the organic has no absorption at 450 nm. This result implies that the photoresponse of the organic-QDs device is contributed from the photoexcitation of the QDs.

In order to further analyze the photoresponse performance of the device, the $I_{\text{D}}-V_{\text{G}}$ characteristics of the device were studied in dark and under 0.14 mW cm^{-2} illumination power intensities (Figure 3b), with a V_{G} sweeping from -60 to 60 V at a fixed V_{D} of 15 V. The threshold voltage (V_{T}) of the device decreases from -26.5 V in dark state to -20.1 V in light state, which is considered to be the result of the increase of photo-excited carriers in the light state. For $V_{\text{D}} = 15 \text{ V}$, the current I_{D} increases almost linearly with V_{DS} (Figure 3a). In this mode, I_{D} can be obtained from the following equation (Section S2, Supporting Information)

$$I_{\text{D}} = \frac{C_i \mu_{\text{lin}} W}{L} \left[(|V_{\text{G}} - V_{\text{T}}|) V_{\text{D}} - \frac{V_{\text{D}}^2}{2} \right] \quad (1)$$

where W is the channel width, L is the channel length, C_i is the capacitance per unit area of the dielectric layer of SiO_2 , and μ_{lin} is the linear regime field-effect mobility. For a large series of

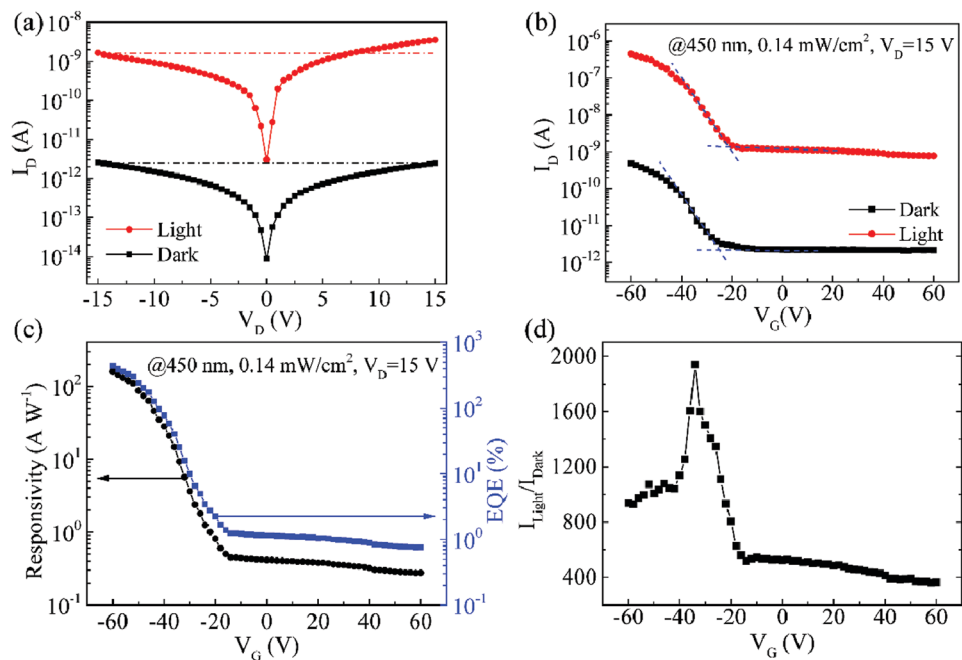


Figure 3. Photoresponse characteristics of the Poly-TPD:PCBM = 1:1 device. a) I_D - V_D characteristics of the photodetectors under irradiation with 450 nm continuous light (0.14 mW cm^{-2}) and in the dark for fixed $V_G = 0 \text{ V}$. b-d) I_D , Responsivity, EQE and I_{Light}/I_{Dark} versus V_G characteristics.

QDs device (>10), the μ_{lin} values in dark state were in the range of $10^{-4}\text{--}10^{-5} \text{ cm}^2 \text{ V}^{-1} \text{ s}^{-1}$. The dark μ_{lin} is very close to that of Poly-TPD and PCBM,^[30,31] which provide further evidence that the dark current of the device is dominated by the organic layer. The corresponding responsivity

$$R = (I_{GD,\text{light}} - I_{GD,\text{dark}})/P_{\text{light}} (\text{A W}^{-1}) \quad (2)$$

is shown in Figure 3c, where $I_{GD,\text{light}}$, $I_{GD,\text{dark}}$, and P_{light} are photocurrent, dark current, and the irradiation light power, respectively. The R is about 0.4 A W^{-1} at $V_G = 0 \text{ V}$, which is comparable to standard silicon detectors. The R increases dramatically with the negative gate voltage applied and reaches 155 A W^{-1} at $V_G = -60 \text{ V}$. The external quantum efficiency (EQE) was obtained by

$$EQE = Rhc/e\lambda \quad (3)$$

where hc/λ is the photon energy, and e is the elementary charge. The EQE exhibits the same gate voltage dependence trend as R (Figure 3c right), reaching 436% at $V_G = -60 \text{ V}$. Figure 3d shows the I_{Light}/I_{Dark} ratio versus the V_G of the device under 0.14 mW cm^{-2} illumination power intensities, with a V_G sweeping from -60 to 60 V at a fixed V_D of 15 V. The I_{Light}/I_{Dark} also shows obvious gate voltage dependence. However, the trend of gate voltage dependence of I_{Light}/I_{Dark} is obviously different from that of R , and there is a maximum of 2000 at $V_G = -34 \text{ V}$. This ultrahigh I_{Light}/I_{Dark} further demonstrates that our device has an ultrasensitive ability in the detection of light.

The $NEP-V_G$ of the device is shown in Figure 4a which is normalized to a 1 Hz bandwidth standard. NEP as low as $1 \times 10^{-16} \text{ W Hz}^{-0.5}$ can be achieved, which is the lowest for the perovskite-based photodetector we know so far.^[3] The NEP in

a device presents all noise sources, including shot noise from dark current, flicker noise, and Johnson noise.^[26,32] To compare with different devices, it is important to provide an area independent figure of merit (D^*)

$$D^* = \sqrt{SAf}/NEP \text{ (Jones)} \quad (4)$$

where S is working area of the device, and Δf is the bandwidth. As shown in Figure 4a (right), the D^* as high as $4.6 \times 10^{13} \text{ Jones}$ can be obtained, which is more than one order of magnitude higher than that of a Si photodetector^[33,34] and better than most reported photodetectors.^[18,35-37] The ultrahigh D^* of the device is mainly benefited from its extremely low dark current, indicating its high sensitivity in detecting light signals.

Figure 4b shows that the R of the photodetector decrease linearly with the increase of laser power when plotted on a log-scale at $V_D = 15 \text{ V}$, $V_G = 0 \text{ V}$. The linear dynamic range of in our device is 7.7 dB, which is much smaller than other perovskite photodetector (154 dB).^[38] This indicates that the photogenerated electron–hole pairs are effectively separated.^[39] Figure 4c gives the time photoresponse behavior of the photodetector, which is measured by periodically turning on and off the 450 nm light at $V_D = 15 \text{ V}$, $V_G = 0 \text{ V}$. The current curve clearly displays two distinct states when the light irradiation is on and off, respectively. As shown in Figure 4d, the rise and decay time are less than 25 ms. The rapid response further indicates the fast separation and efficient extraction of photo-carriers from CsPbBr_3 QDs. The performance of photodetector based on the CsPbBr_3 materials are summarized in Table 1. We can find that the organic-modulated QDs photodetectors have excellent photoresponse properties, which would have great potential as photodetectors.

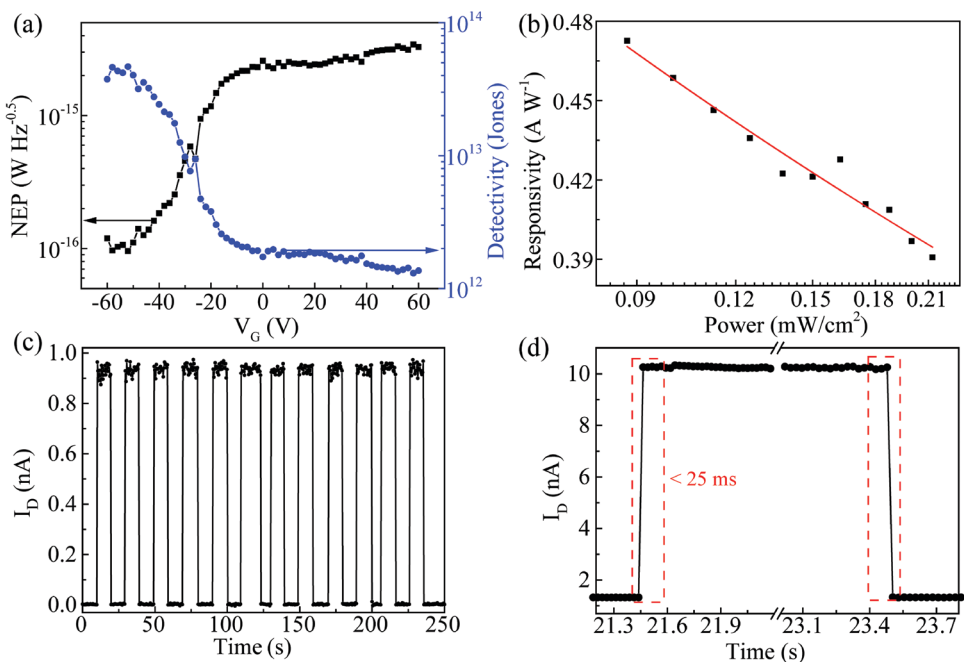


Figure 4. NEP, Detectivity, power-dependent, and On/off characteristics of the photodetectors. a) NEP and detectivity versus V_G characteristics of the 1:1 device. b) The R of the photodetector as a function of power intensity at $V_G = 0$ V. c) Time-resolved photoresponse was measured at 450 nm, which indicates a highly stable and reversible response of the photodetectors. d) Temporal response exhibits fast photoswitching.

3. Discussion

It is worth noting that the photoresponse ability of the QDs photodetector can be effectively modulated by organic blend materials of poly-TPD and PCBM through varying their weight ratio. As shown in Figure 2c,d, although the photocurrent increases with the increase of PCBM, the dark current also increases greatly. The corresponding D^* is 2.84×10^{12} (2:1), 3.32×10^{13} (1:1), and 1.04×10^{13} (1:2) Jones, respectively. At the same time, the photocurrent transfers from a nonlinear voltage dependence (heterojunction structure) to symmetrical linear voltage dependence (ohmic contact) with the increase of PCBM (Figure 2c). To light the origin of this interesting evolution, the energy band diagrams of QDs and blend organic need to be presented accurately. Here, the ultraviolet photoelectron spectroscopy (UPS, Figure 5a) combined with absorption spectra (Figure 5b) are used to determine the energy level of the stacked device (Figure S8 shows the UPS of QDs, Supporting Information). UPS shows occupied electronic states and thus

provided information on the Fermi level (high-binding-energy cutoff) and valence band edge (low-binding-energy-cutoff).^[44,45] The energy E_{CB} of the conduction band can be approximated by adding the electronic transition gap E_g . The schematic of band structure at organic and QDs interface can be obtained as the content of organic components changes.

As the ratio of Poly-TPD to PCBM varied from 2:1, 1:1 to 1:2, the conduction band energy offset between QDs and organic blend layers gradually decreases from 0.66, 0.33 to -0.03 eV, and the valance band energy offset have been consistently decreased from 0.04, -0.28 to -0.63 eV, respectively (Figure 5c). Here, we also found that the dark current of single-layer 2:1 organic photodetector displays slightly larger value than those of the other two samples (Figure S9, Supporting Information), which implies that the 2:1 organic material has better conductivity. If photogenerated electron–hole pairs in QDs can be transferred equivalently through the interface to the organic layer, the 2:1 sample should exhibit a larger photocurrent due to its smaller hole offset and greater conductivity.

Table 1. The performance of photodetector based on the CsPbBr₃ materials.

Device structure	Responsivity [R, A W ⁻¹]	Detectivity [D*, Jones]	Noise equivalent power [NEP]	Response time	Ref.
PTAA/PEIE/CsPbBr ₃ /PCBM/BCP	0.3	6.0×10^{12}	3.5×10^{-14}	62 ns	[6]
CsPbBr ₃ QDs/Graphene	2×10^4	8.6×10^{10}	—	≈ s	[40]
Au/CsPbBr ₃ film/Au	≈0.2	6.1×10^{10}	—	≈2 ms	[41]
Au/CsPbBr ₃ nanowire/Au	2.4×10^3	—	—	≈0.5 ms	[42]
Au/CsPbBr ₃ single crystals/Au	2.1	—	—	≈ s	[43]
Poly-TPD:PCBM/CsPbBr ₃ QDs/ Poly-TPD:PCBM	0.4	4.6×10^{13}	1×10^{-16}	<25 ms	This work

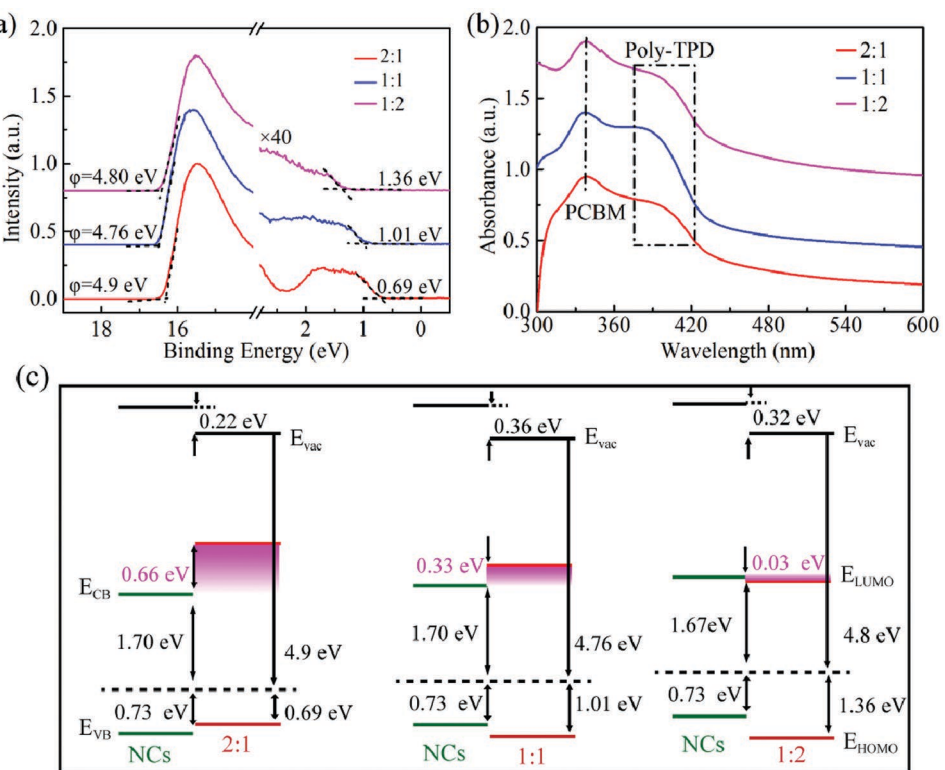


Figure 5. Energy bands of the organic-QDs photodetector. a) UPS spectra of the mixed-organic materials. b) Absorption spectra of the mixed organic materials. c) Schematic energy-level diagram of CsPbBr_3 QDs and organic materials.

However, in fact, the 1:2 sample exhibits a larger photocurrent. This indicates that the electron provides more contribution to the photocurrent than holes. As a result, the photogenerated electrons in CsPbBr_3 QDs could effectively dissociate in the energy favorable interface of QDs and organic layers, and free electrons could be quickly transported through the conductive organic layers and collected to their respective Au electrode, which agrees well with Figure 2c where photocurrent has been consistently increased when the ratio changes from 2:1, 1:1, and 1:2. Therefore, this can also explain that the organic materials with increasing PCBM have successfully modulated the stacked QD photodetectors from heterojunction (higher energy barrier) to ohmic contact (nearly flat barrier). In the meantime, energy offset of QDs and organic layers could effectively block the reverse leakage current of photodetectors, thus the 1:2 photodetector with the lowest energy offset of 0.03 eV has the highest dark current as shown in Figure 2d. Correspondingly, the as-prepared organic/QDs/organic photodetector has the best device performance for 1:1 ratio of poly-TPD and PCBM in terms of optimized photocurrent and dark current.

To obtain a quantitative picture of the carrier dynamics at CsPbBr_3 QDs/blend organic interfaces, the PL decay of QDs only and organic/QDs/organic thin films were measured by using time correlated single photon counting measurements excited by a 90 ps pulsed laser diode at 3.2 eV (405 nm). By fitting the data in Figure 6a with a biexponential process, the relaxation time for the two different sample consisted of a fast component with 0.71 and 0.93 ns, followed by a slow component with 4.09 and 4.7 ns. The faster relaxation process is likely

caused by interband relaxation. And, this process plays a dominant role in the relaxation time since the weight factor is 96% for single QDs layer sample and 90% for multilayer devices (1:1 sample). The relative faster relaxation process for the multilayer devices indicated that there is an effective charge separation process from the QDs to the organic blend layer.

In order to further reveal the carrier dynamics process, the ultrafast transient absorption spectroscopy (TAS) measurements were conducted on the pure QDs films and organic/QDs/organic multilayer film. The TAS technique is considered to be a powerful tool for extracting information regarding charge carrier transfer, recombination dynamics, and relaxation time in photoactive thin films.^[46,47] Herein, a pump pulse at 400 nm was used to excite the quartz/organic/QDs/organic layer, and induced absorption changes (ΔAbs), as a function of both wavelength and time, were recorded by a white light continuum probe pulse variably delayed with respect to the pump pulse. The TA spectra (Figure 6b) at delay time of the organic/QDs/organic showed a ground state bleach feature at ≈ 510 nm and excited state absorption at ≈ 480 and 527 nm which is found to attenuate with time from 1 ps to 5 ns. The TA spectra of the pure QDs is located in Figure S10 (Supporting Information). To get the kinetic trace of the QDs in the organic/QDs/organic structure, we exclude the excited state absorption signal of the organic from the experimental data. By comparing the difference between kinetic traces of the pure QDs and QDs in the organic/QDs/organic structure (Figure 6c), we could get the charge transfer kinetics in the interface between QDs and organic layers (Figure 6d). By fitting the charge transfer kinetics

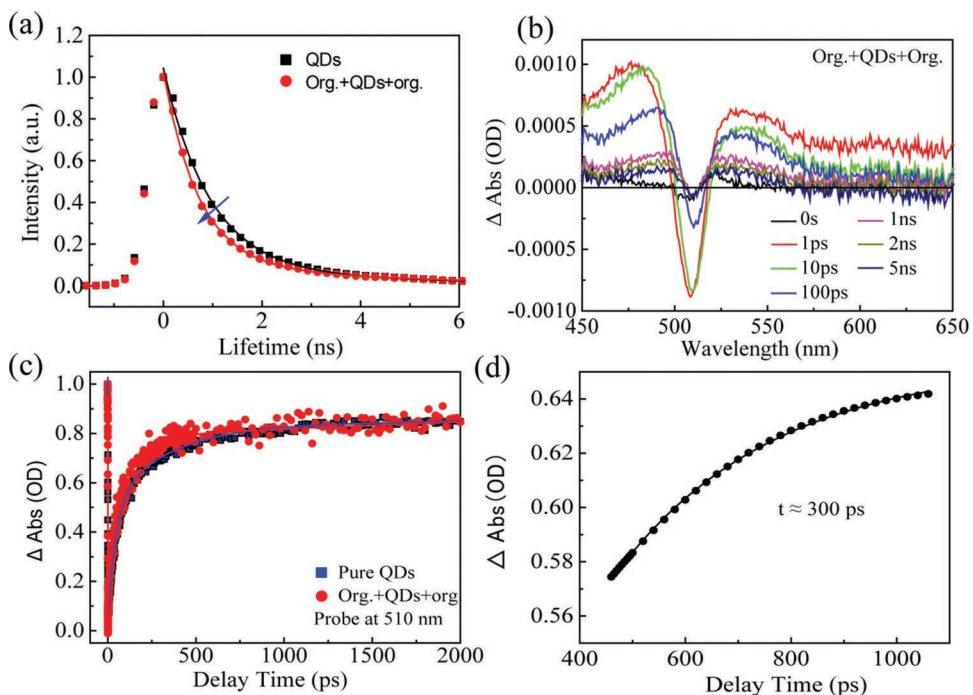


Figure 6. Photocarrier dynamic of the organic-QDs device. a) PL decay curves of pure QDs film and organic/QDs/organic structure. b) TAS of the organic/QDs/organic multilayer film at indicated delay time from 0 s to 5 ns. c) Transient absorption kinetics of the multilayer film and pure QDs film. d) Charge transfer kinetics in organic/QDs/organic multilayer film. The solid line was fit using a single exponential. For all ultrafast optical measurements, the excitation source was an 80 fs pulsed laser with a repetition rate of 1 kHz.

data, we can obtain an $\approx 300 \text{ ps}$ charge transport time from QDs to organic layer, indicating ultrafast charge separation occurring at the organic-QDs interfaces. The faster charge transport time is in agreement with the obtained PL characteristics, in which significant quenching upon the addition of organic blend layer as the electron/hole transport layers indicates a faster hole/electron extraction (Figure 2a).

4. Conclusion

In summary, an adjustable hybrid high-performance organic-QDs photodetector was demonstrated. By using M7100 as an effective protective layer for QD film, we can solve the biggest challenge in the all-solution process: the orthogonality between quantum dot layer and organic layer solvents, resulting smooth and continuous interfaces between CsPbBr_3 QDs and organic films. Interestingly, the organic materials with increasing PCBM have successfully modulated the stacked QD photodetectors from heterojunction (higher energy barrier) to ohmic contact (nearly flat barrier). The TA spectrum studies reveal that faster charge transfer time ($\approx 300 \text{ ps}$) and decay dynamics when the organic blend layers is employed, which potentially account for the enhanced photocurrent generation. In addition, the ordered nanocrystalline interface with extended heterojunction of QDs and organic blend films has lowered trap-assisted carrier recombination, substantially reducing dark current. The photodetectors exhibit outstanding photoresponse properties in terms of detectivity ($4.6 \times 10^{13} \text{ J}$), NEP ($1 \times 10^{-16} \text{ W Hz}^{-0.5}$), and $I_{\text{Light}}/I_{\text{Dark}}$ ratio (2×10^3). We anticipate that our results

will be a starting point for further research, leading to high-performance, all-solution-processed, and organic-nanocrystals modulated photodetector ideal for next-generation light detection technologies.

5. Experimental Section

CsPbBr_3 QDs Synthesis: The CsPbBr_3 QDs were fabricated according to a chemical solution route similar to a previously reported approach.^[48] First, a Cs(OA)_2 solution was synthesized by dissolving CsCO_3 powder (2.394 mmol, 99.9%) in oleic acid (OA, 1.25 mL, 90%), and octadecene (ODE, 20 mL, 90%) at 25 °C for 20 min and then increased to 150 °C for 30 min under an N_2 flow with a stirring speed of 500 rpm to exclude the moisture in the reaction reagent. In another three-neck flask, ODE (10 mL, 90%) and PbBr_2 (0.375 mmol, 99.999%) were mixed and dried under vacuum at 110 °C for 30 min. Then, dried OA (1 mL, 90%) and dried oleylamine (1 mL, 90%) were injected into the mixed solution at 110 °C under N_2 . The temperature for mixture was heated to 160 °C for 10 min under a N_2 flow. Subsequently, the Cs(OA)_2 solution (0.8 mL) was quickly injected into the reaction system. The reaction solution was cooled using an ice-water bath after 5 s. The CsPbBr_3 QDs in crude solution were separated by centrifuging at 11 000 rpm for 10 min and cleaned using acetone/hexane mixture solution. After centrifugation, the CsPbBr_3 QDs were redispersed in octane.

Device Fabrication: Heavily p-doped Si wafers with 300 nm of SiO_2 layer were used as substrates. The substrates were cleaned by ultrasonication for 20 min in acetone, isopropanol, deionized water, and finally dried by N_2 . The Poly-TPD and PCBM were first dissolved in chlorobenzene solvent with a mass concentration of 10 mg mL^{-1} . Furthermore, organic materials with different material compositions were obtained. The spin-casting processes were performed in Ar gas glove box. The first layer organic materials were spin coated at 3000 rpm for 50 s, followed by annealing at 110 °C for 30 min. The QDs layers were spin coated from

a 15 mg mL⁻¹ octane solution at 1500 rpm for 45 s and annealed at 85 °C for 20 min. Then, the M7100 layers were spin coated at 1500 rpm for 30 s and no heat treatment. About 2 min later, the last layer organic materials were spin coated at 4000 rpm for 40 s, followed by annealing at 95 °C for 30 min. After that, the samples were transferred to a high-vacuum evaporation chamber to deposit the Cr/Au anode. Channel length and width were determined by optical microscopy.

Device Characterization: TEM images of QDs were recorded using a JEOL 2010 TEM equipped with a SC1000 ORIUS CCD camera operating at 120 kV. The crystal structure of the QDs was examined by high-resolution X-ray diffraction (Bede D1 System) with the Cu K α X-ray source (1.54 Å wavelength) operating at 40 kV and 40 mA. UV-vis absorption spectra for QDs thin films on quartz substrates were collected using a Cary 60 UV-vis spectrometer (Agilent Technologies). Cross-sectional SEM studies of the device were conducted on an FEI Magellan 400 XHR SEM. All I-V measurements were carried out with a Keithley 4200 SCS at room temperature. The noise measurements were performed by using an SR570 low-noise current amplifier and a Hewlett Packard 89441 vector signal analyzer. UPS spectra are collected using an Omicron ultrahigh vacuum system with a base pressure of 10⁻¹⁰ mbar. TA spectra and dynamic were measured in a standard pump-probe configuration using a LabView-controlled home-build setup.

Supporting Information

Supporting Information is available from the Wiley Online Library or from the author.

Acknowledgements

This work was supported financially by the Shenzhen Municipal Development and Reform Commission, and New Energy Technology Engineering Laboratory (Grant No. SDRC [2016]172). The authors thank MingQiang Liu for technical support on thermal evaporation of the metal electrode. The authors also thank Qiang Su and Prof. Shuming Chen for the help on the PL lifetime measurement.

Conflict of Interest

The authors declare no conflict of interest.

Keywords

detectivity, organic materials, perovskite quantum dots, photodetectors, solution-processed

Received: October 14, 2019

Revised: November 13, 2019

Published online: December 17, 2019

- [1] S. Goossens, G. Navickaite, C. Monasterio, S. Gupta, J. J. Piqueras, R. Perez, G. Burwell, I. Nikitskiy, T. Lasanta, T. Galan, E. Puma, A. Centeno, A. Pesquera, A. Zurutuza, G. Konstantatos, F. Koppens, *Nat. Photonics* **2017**, *11*, 366.
- [2] F. H. L. Koppens, T. Mueller, P. Avouris, A. C. Ferrari, M. S. Vitiello, M. Polini, *Nat. Nanotechnol.* **2014**, *9*, 780.
- [3] H. Wang, D. H. Kim, *Chem. Soc. Rev.* **2017**, *46*, 5204.
- [4] C. Livache, B. Martinez, N. Goubet, C. Greboval, J. L. Qu, A. Chu, S. Royer, S. Ithurria, M. G. Silly, B. Dubertret, E. Lhuillier, *Nat. Commun.* **2019**, *10*, 2125.
- [5] J. Feng, C. Gong, H. Gao, W. Wen, Y. Gong, X. Jiang, B. Zhang, Y. Wu, Y. Wu, H. Fu, L. Jiang, X. Zhang, *Nat. Electron.* **2018**, *1*, 404.
- [6] C. Bao, J. Yang, S. Bai, W. Xu, Z. Yan, Q. Xu, J. Liu, W. Zhang, F. Gao, *Adv. Mater.* **2018**, *30*, 1803422.
- [7] S. Cai, X. Xu, W. Yang, J. Chen, X. Fang, *Adv. Mater.* **2019**, *31*, 1808138.
- [8] S. Li, Y. Zhang, W. Yang, X. Fang, *Adv. Mater. Interfaces* **2019**, *6*, 1900669.
- [9] Y. Li, Z. Shi, L. Lei, S. Li, D. Yang, D. Wu, T. Xu, Y. Tian, Y. Lu, Y. Wang, L. Zhang, X. Li, Y. Zhang, G. Du, C. Shan, *Adv. Mater. Interfaces* **2019**, *6*, 1900188.
- [10] Y. Li, Z. Shi, W. Liang, L. Wang, S. Li, F. Zhang, Z. Zhuang Ma, Y. Wang, Y.-Z. Tian, D. Wu, *Mater. Horiz.* **2019**, <https://doi.org/10.1039/c9mh01371g>.
- [11] X. Xu, J. Chen, S. Cai, Z. Long, Y. Zhang, L. Su, S. He, C. Tang, P. Liu, H. Peng, *Adv. Mater.* **2018**, *30*, 1803165.
- [12] Z. Yang, M. Wang, H. Qiu, X. Yao, X. Lao, S. Xu, Z. Lin, L. Sun, J. Shao, *Adv. Funct. Mater.* **2018**, *28*, 1705908.
- [13] D. P. Li, C. Y. Lan, A. Manikandan, S. Yip, Z. Y. Zhou, X. G. Liang, L. Shu, Y. L. Chueh, N. Han, J. C. Ho, *Nature* **2019**, *569*, E10.
- [14] D. V. Talapin, J. S. Lee, M. V. Kovalenko, E. V. Shevchenko, *Chem. Rev.* **2010**, *110*, 389.
- [15] D. Yu, C. J. Wang, P. Guyot-Sionnest, *Science* **2003**, *300*, 1277.
- [16] N. Goubet, C. Livache, B. Martinez, X. Z. Xu, S. Ithurria, S. Royer, H. Cruguel, G. Patriarche, A. Ouerghi, M. Silly, B. Dubertret, E. Lhuillier, *Nano Lett.* **2018**, *18*, 4590.
- [17] A. Yousefian, N. A. Killilea, M. Sytnyk, P. Maisch, K. C. Tam, H. J. Egelhaaf, S. Langner, T. Stubhan, C. J. Brabec, T. Rejek, M. Halik, K. Poulsen, J. Niehaus, A. Kock, W. Heiss, *ACS Nano* **2019**, *13*, 2389.
- [18] M. G. Gong, R. Sakidja, R. Goul, D. Ewing, M. Casper, A. Stramel, A. Elliot, J. Z. Wu, *ACS Nano* **2019**, *13*, 3714.
- [19] D. J. Norris, *Nat. Photonics* **2019**, *13*, 230.
- [20] K. S. Cho, K. Heo, C. W. Baik, J. Y. Choi, H. Jeong, S. Hwang, S. Y. Lee, *Nat. Commun.* **2017**, *8*, 9.
- [21] R. Saran, R. J. Curry, *Nat. Photonics* **2016**, *10*, 81.
- [22] J. S. Lee, M. V. Kovalenko, J. Huang, D. S. Chung, D. V. Talapin, *Nat. Nanotechnol.* **2011**, *6*, 348.
- [23] Y. Liu, M. Gibbs, J. Puthussery, S. Gaik, R. Ihly, H. W. Hillhouse, M. Law, *Nano Lett.* **2010**, *10*, 1960.
- [24] G. Konstantatos, M. Badioli, L. Gaudreau, J. Osmond, M. Bernechea, F. P. G. de Arquer, F. Gatti, F. H. L. Koppens, *Nat. Nanotechnol.* **2012**, *7*, 363.
- [25] K. Szendrei, F. Cordella, M. V. Kovalenko, M. Boberl, G. Hesser, M. Yarema, D. Jarzab, O. V. Mikhnenco, A. Gocalinska, M. Saba, F. Quochi, A. Mura, G. Bongiovanni, P. W. M. Blom, W. G. Heiss, M. A. Loi, *Adv. Mater.* **2009**, *21*, 683.
- [26] Y. J. Fang, A. Armin, P. Meredith, J. S. Huang, *Nat. Photonics* **2019**, *13*, 1.
- [27] Y. Chen, Y. Chu, X. Wu, W. Ou-Yang, J. Huang, *Adv. Mater.* **2017**, *29*, 1704062.
- [28] D. Muhlbacher, M. Scharber, M. Morana, Z. G. Zhu, D. Waller, R. Gaudiana, C. Brabec, *Adv. Mater.* **2006**, *18*, 2884.
- [29] X. Y. Yang, Y. Divayana, D. W. Zhao, K. S. Leck, F. Lu, S. T. Tan, A. P. Abiyasa, Y. B. Zhao, H. V. Demir, X. W. Sun, *Appl. Phys. Lett.* **2012**, *101*, 4.
- [30] T. J. Savenije, J. E. Kroese, M. M. Wienk, J. M. Kroon, J. M. Warman, *Phys. Rev. B* **2004**, *69*, 11.
- [31] X. L. Dai, Z. X. Zhang, Y. Z. Jin, Y. Niu, H. J. Cao, X. Y. Liang, L. W. Chen, J. P. Wang, X. G. Peng, *Nature* **2014**, *515*, 96.
- [32] J. R. Manders, T. H. Lai, Y. B. An, W. K. Xu, J. Lee, D. Y. Kim, G. Bosman, F. So, *Adv. Funct. Mater.* **2014**, *24*, 7205.
- [33] L. T. Dou, Y. Yang, J. B. You, Z. R. Hong, W. H. Chang, G. Li, Y. Yang, *Nat. Commun.* **2014**, *5*, 6.
- [34] X. Gong, M. H. Tong, Y. J. Xia, W. Z. Cai, J. S. Moon, Y. Cao, G. Yu, C. L. Shieh, B. Nilsson, A. J. Heeger, *Science* **2009**, *325*, 1665.

- [35] L. Wang, X. Zou, J. Lin, J. Jiang, Y. Liu, X. Liu, X. Zhao, Y. F. Liu, J. C. Ho, L. Liao, *ACS Nano* **2019**, *13*, 4804.
- [36] A. L. Li, Q. X. Chen, P. P. Wang, Y. Gan, T. L. Qi, P. Wang, F. D. Tang, J. Z. Wu, R. Chen, L. Y. Zhang, Y. P. Gong, *Adv. Mater.* **2019**, *31*, 1805656.
- [37] C. Chen, L. Gao, W. R. Gao, C. Y. Ge, X. Du, Z. Li, Y. Yang, G. D. Niu, J. Tang, *Nat. Commun.* **2019**, *10*, 1927.
- [38] W. L. Tsai, C. Y. Chen, Y. T. Wen, L. Yang, Y. L. Cheng, H. W. Lin, *Adv. Mater.* **2019**, *31*, 1900231.
- [39] Y. Wen, L. Yin, P. He, Z. X. Wank, X. K. Zhang, Q. S. Wang, T. A. Shifa, K. Xu, F. M. Wang, X. Y. Zhan, F. Wang, C. Jiang, J. He, *Nano Lett.* **2016**, *16*, 6437.
- [40] J.-h. Chen, Q. Jing, F. Xu, Y.-q. Lu, *Optica* **2017**, *4*, 835.
- [41] X. Li, D. Yu, F. Cao, Y. Gu, Y. Wei, Y. Wu, J. Song, H. Zeng, *Adv. Funct. Mater.* **2016**, *26*, 5903.
- [42] M. Shoaib, X. Zhang, X. Wang, H. Zhou, T. Xu, X. Wang, X. Hu, H. Liu, X. Fan, W. Zheng, *J. Am. Chem. Soc.* **2017**, *139*, 15592.
- [43] J. H. Cha, J. H. Han, W. Yin, C. Park, Y. Park, T. K. Ahn, J. H. Cho, D.-Y. Jung, *J. Phys. Chem. Lett.* **2017**, *8*, 565.
- [44] P. R. Brown, D. Kim, R. R. Lunt, N. Zhao, M. G. Bawendi, J. C. Grossman, V. Bulovic, *ACS Nano* **2014**, *8*, 5863.
- [45] J. Endres, M. Kulbak, L. F. Zhao, B. P. Rand, D. Cahen, G. Hodes, A. Kahn, *J. Appl. Phys.* **2017**, *121*, 035304.
- [46] B. D. Zhao, S. Bai, V. Kim, R. Lamboll, R. Shivanna, F. Auras, J. M. Richter, L. Yang, L. J. Dai, M. Alsari, X. J. She, L. S. Liang, J. B. Zhang, S. Lilliu, P. Gao, H. J. Snaith, J. P. Wang, N. C. Greenham, R. H. Friend, D. W. Di, *Nat. Photonics* **2018**, *12*, 783.
- [47] K. F. Wu, G. J. Liang, Q. Y. Shane, Y. P. Ren, D. G. Kong, T. Q. Lian, *J. Am. Chem. Soc.* **2015**, *137*, 12792.
- [48] L. Protesescu, S. Yakunin, M. I. Bodnarchuk, F. Krieg, R. Caputo, C. H. Hendon, R. X. Yang, A. Walsh, M. V. Kovalenko, *Nano Lett.* **2015**, *15*, 3692.